Entropic Control of Bonding, Guided by Chemical Pressure: Phase Transitions and 18-*n*+*m* Isomerism of $IrIn_3$

Amber Lim and Daniel C. Fredrickson*

Department of Chemistry, University of Wisconsin-Madison, 1101 University Avenue, Madison, Wisconsin, 53706, United States

ABSTRACT: As with other electron counting rules, the 18-*n* rule of transition metal-main group (T-E) intermetallics offers a variety of potential interatomic connectivity patterns for any given electron count. What leads a compound to prefer one structure over others that satisfy this rule? Herein, we investigate this question as it relates to the two polymorphs of $IrIn_3$: the high-temperature $CoGa_3$-type and the low-temperature $IrIn_3$-type forms. DFT-reversed approximation Molecular Orbital (raMO) analysis reveals that both structures can be interpreted in terms of the 18-*n* rule but with different electron configurations. In the $IrIn_3$ type, the Ir atoms obtain largely independent 18-electron configurations, while in the $CoGa_3$ type, Ir-Ir isolobal bonds form as 1 electron/Ir atom is transferred to In-In interactions. The presence of a deep pseudogap for the $CoGa_3$ type, but not for the $IrIn_3$ type, suggests it is electronically preferred. DFT-Chemical Pressure (CP) analysis shows that atomic packing provides another distinction between the structures. While both involve tensions between positive Ir-In CPs and negative In-In CPs, which call for the expansion and contraction of the structures, respectively, their distinct spatial arrangements create very different situations. In the $CoGa_3$ type, the positive CPs create a framework that holds open large void spaces for In-based electrons (a scenario suitable for relatively small T atoms), while in the $IrIn_3$ type the pressures are more homogenously distributed (a better solution for relatively large T atoms). The open spaces in the $CoGa_3$ type result in quadrupolar CP features, a hallmark of low-frequency phonon modes and suggestive of higher vibrational entropy. Indeed, phonon band structure calculations for the two $IrIn_3$ polymorphs indicate that the phase transition between them can largely be attributed to the entropic stabilization of the $CoGa_3$-type phase due to soft motions associated with its CP quadrupoles. These CP-driven effects illustrate how the competition between global and local packing can shape how a structure realizes the 18-*n* rule and how the temperature can influence this balance.

1. INTRODUCTION

One need only consider the allotropes of phosphorus,[1-5] the diversity of fullerenes and carbon nanotubes,[6-8] or the richness of Zintl phases[9-14] to see that electron counting rules, such as the octet rule, do not predict specific structures. Instead, they provide guidelines by which a variety of geometries can be constructed. For molecular chemistry, this offers a wide range of potential compounds for synthesis. For traditional solid state chemistry, however, where high temperature synthetic conditions mean that only the thermodynamic products are obtained, it raises a question. What determines the observed structure of a solid state material when multiple candidate structures offer reasonable bonding schemes from the viewpoint of the electronic structure?

In this Article, we explore this question through the theoretical analysis of the two polymorphs of $IrIn_3$ (Figure 1).[15-17] These two structures conform to the 18-*n*+*m* rule, which connects the electron counts of transition metal (T)-main group intermetallics (E) to their structural arrangements.[18] In this scheme, 18-*n* electrons are needed for each T atom in a structure to achieve a closed-shell configuration, where *n* is the number of electron pairs it shares with other T atoms in multicenter interactions. Any extra electrons in the structure are then involved in E-E interactions, such that the overall electron count is 18-*n*+*m* per T atom, with *m* denoting the number of electrons per T atom associated with the E sublattice. This rule correlates electron count and structural connectivity, unlocking different possible combinations of *n* and *m* for each electron count.

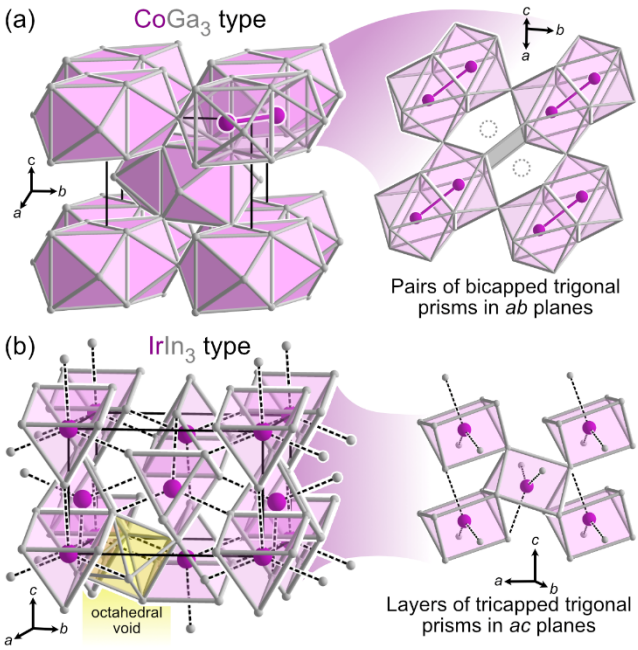

Figure 1. The structures of the two polymorphs of $IrIn_3$. (a) The high-temperature $CoGa_3$-type form contains dumbbells of Ir atoms (purple) centered in paired bicapped trigonal prism units, with empty spaces arising between units (highlighted with dotted circles). (b) In the low-temperature $IrIn_3$-type form, Ir atoms occupy tricapped trigonal prisms of In, buffered by distorted octahedral voids (yellow). The Ir@In_9 prisms run along the *ac*-plane in vertex- and edge-sharing layers.

For both polymorphs of $IrIn_3$, the overall electron count given by the stoichiometry is 18 electrons/Ir atom. However, geometrical inspection suggests these electrons are distributed differently through the structure, corresponding to different (n,m) configurations. In the high-temperature $CoGa_3$-type polymorph (Figure 1a), the Ir atoms comprise dumbbells, suggesting the presence of isolobal bonds, such that n=1, and allowing In-In bonding to form elsewhere, such that m=1. For the low-temperature $IrIn_3$-type structure (Figure 1b), on the other hand, the Ir atoms are essentially isolated from each other, suggesting that (n,m)=(0,0).

What factors determine the relative stability of these different (n,m) configurations in this system? Clues are offered by previous studies on Ir-In and related systems: For $IrIn_3$, the $CoGa_3$-type phase readily forms as the high-temperature phase,[15,17] while at lower temperatures, full conversion to the $IrIn_3$-type is never achieved.[16] In fact, $IrGa_3$ is the only other TE_3 compound composed of Group 9 and Group 13 elements that exhibits analogous polymorphism.[19] Other members of the family, $CoGa_3$, $CoIn_3$, $RhIn_3$, and $RhGa_3$, occur solely in the $CoGa_3$ type.[17,20,21] The prominence of the $CoGa_3$ type is consistent with the observation that this structure minimizes antibonding interactions near the Fermi energy at 18 electrons/T atom.[22]

It remains unclear, however, why under certain conditions the $IrIn_3$-type is preferred. Here, we combine DFT-reversed approximation Molecular Orbital (DFT-raMO) analysis[23] and DFT-Chemical Pressure (DFT-CP) analysis[24-27] to determine how the electronic structure and atomic packing interact to shape the structural preferences in these systems. We will see that the different (n,m) configurations for the two polymorphs have distinct spatial requirements and are adapted for different T/E atomic size ratios. In addition, one of these polymorphs exhibits more pronounced CP quadrupoles, signatures of soft modes of atomic motion, leading to it being favored at higher temperatures for entropic reasons. The emerging picture offers a framework for understanding how T-E intermetallic systems navigate potential (n,m) configurations as they adopt their ground state geometries.

2. EXPERIMENTAL SECTION

Electronic Density of States and Crystal Orbital Hamilton Population analysis. Electronic density of states (DOS) distributions for $IrIn_3$ in the $CoGa_3$ and $IrIn_3$ structure types were calculated with the *Vienna Ab-initio Simulation Package* (*VASP*).[28-30] The geometries were optimized, first with the cell held rigid while the atomic positions were relaxed, and then with the release of all geometric parameters. The calculations employed the generalized gradient approximation (GGA) and the Projected Augmented Wave (PAW) potentials provided with the package,[31,32] and Γ-centered 9×9×9 k-point meshes. They were performed in high-precision mode with an energy cutoff of 263.6 eV and considered converged at energy differences of 1×10^{-5} eV for electronic steps and 1×10^{-4} eV for ionic steps. After the geometry optimizations, single-point calculations were performed to obtain the DOS distribution, with fineness of the k-point meshes increased to 15×15×15 to obtain convergence in the details and features of the DOS distributions. The wavefunctions from the *VASP* calculation were used as input for Crystal Orbital Hamilton Population (COHP) analysis.[33-35] COHP curves (for $CoGa_3$-type $IrIn_3$) and projected DOS distributions were generated with the *Local-Orbital Basis Suite Towards Electronic-Structure Reconstruction* (*LOBSTER*)[36,37] software using the Ir 6s, 5d, and 6p, and In 5s and 5p basis functions. The *Electrum.jl* package was used in the processing and plotting of the electronic DOS distributions.[38]

DFT-raMO analysis. Optimized geometries from the single-point calculations in *VASP* were used in the preparatory static calculations for DFT-raMO analysis. To obtain wavefunction information over the whole Brillouin zone, calculations were performed using a 2×2×2 k-point mesh and without symmetry considerations. Wavefunction information was extracted with the *WaveTrans* program[39] and imported into the *DFT-raMO* software.[23] In each cycle, an overlap matrix between the current basis set of occupied functions and the target function (constructed from linear combinations of parameterized Slater-type orbitals) was calculated and subsequently used to generate the raMO Hamiltonian matrix for the target. This matrix was then diagonalized to obtain a reconstructed version of the target function as well as remainder functions, which were returned to the basis set and used for generating subsequent targets.

The quality and degree of localization of the raMOs across the series was monitored with the P_{sphere} metric, the fraction of the raMO's electron density within a sphere of a defined radius (r_{sphere}) centered on the target function.[40] raMOs with relatively high P_{sphere} values were considered occupied by electron pairs. When P_{sphere} values are inconsistent across a series or relatively low, the raMOs are manually inspected for the resemblance to the target function. raMOs rejected at this step were not assigned electrons and were returned to the basis set for use in future reconstructions.

DFT-Chemical Pressure Analysis. The DFT-Chemical Pressure (DFT-CP) schemes were generated for $IrIn_3$, $CoIn_3$, and $IrGa_3$ in both the $CoGa_3$ and $IrIn_3$ structure types, based on the non-spin-polarized ground state electronic structures calculated with the *ABINIT* package, using the Local Density Approximation (LDA) and Hartwigsen-Goedecker-Hutter (HGH) norm-conserving pseudopotentials[41-45] (the standard platform for DFT-CP calculations). The systems were first geometrically optimized in a two-step method in which atomic positions were first allowed to relax, and then both atomic positions and cell parameters were released. The calculations were considered converged at energy differences of 10^{-5} eV (electronic steps) and the forces on the atoms are below 2.6×10^{-3} eV/Å (ionic steps).

Single-point calculations were then performed on the equilibrium, slightly expanded, and slightly contracted geometries (linear scale ±0.5%) to obtain the kinetic energy densities, electron densities, and local components of the Kohn-Sham potentials.[25] Contributions from the Ewald energy and E_α components were spatially distributed to achieve self-consistency between net pressures obtained from the contact volumes and atomic cells, as obtained from the iterative binary Hirschfeld scheme.[26] CP maps were constructed using the core-unwarping procedure[46] and pressures within contact volumes were averaged and projected onto spherical harmonics centered on the atomic sites. The CP schemes were visualized with l_{max} = 4 for the spherical harmonics using the in-house program *figuretool2*.

Spin-orbit coupling. Calculations of the electronic DOS distributions and DFT-Chemical Pressures schemes of $CoGa_3$- and $IrIn_3$-type $IrIn_3$ were also prepared based on ground state electronic structures calculations with spin-orbit coupling activated in the ABINIT program, as described in Ref. 47. These resulting plots are presented in the Supporting Information, where it can be seen that the spin-orbit coupling has little effect on the features of the DOS near the Fermi energy or the CP schemes.

Phonon band structure calculations. The phonon band structures of $IrIn_3$ in the $CoGa_3$ and $IrIn_3$ structure types were calculated using the linear response method with the *ABINIT* package.[41-45] First, the ground state wavefunctions of each system were calculated for the equilibrium geometry (with LDA-HGH pseudopotentials) using a Γ-centered 5×5×5 k-point grid. Non-self-consistent calculations were then performed at q-space (reciprocal space for phonons) points, where the linear response for displacements of the atoms in 3D was obtained. The *mrgddb* and *anaddb* utilities were used to calculate the interatomic force constants, phonon band structures, phonon density of states, and vibrational entropy as a function of temperature from the linear response calculations. The phonon density of states and band structures were processed and plotted with *Electrum.jl*. Phonon modes were extracted at the Γ-point and plotted using *figuretool2*.

3. RESULTS & DISCUSSION

3.1. Preliminary Electronic Analysis of 18-*n*+*m* Isomerism in $IrIn_3$. The 18-*n* rule provides a framework for interpreting the structures of the two polymorphs of $IrIn_3$. Here, transition metal

(T) atoms are viewed as achieving closed-shell 18-electron configurations through the covalent sharing of electron pairs with other T atoms. These shared electrons are held in isolobal bonds, multicenter bonding functions that share the nodal and symmetry properties of direct T-T interactions but include contributions from bridging main group (E) atoms. When the T atoms participate in *n* isolobal bonds, each requires 18-*n* electrons for a filled octadecet. Any remaining valence electrons in the compound are then associated with the E atoms, often in E-E bonds. The overall valence electron concentration for the compound is then 18-*n*+*m* per T atom, where *n* is the average number of isolobal bonds for the T atoms and *m* is the number of electrons per T atom belonging to E-E interactions.

A notable feature here is that for any electron concentration, a range of (*n*,*m*) pairs can be envisioned. The geometries of $IrIn_3$'s polymorphs represent examples of this potential for diversity. In the high-temperature $CoGa_3$-type form (space group $P4_2/mnm$), the Ir atoms are centered in bicapped trigonal prisms of In atoms that are paired through shared square faces (Figure 1a). These pairs link through the sharing of capping atoms in the *ab* layer and shared trigonal prism corners along *c*, creating a pattern in which Ir-filled pairs of trigonal prisms alternate with pairs of vacant trigonal prisms (dotted circles).

In this arrangement, the Ir atoms occur as dumbbells, each with the apparent presence of an isolobal bond (*n*=1). To fulfill the 18-*n*+*m* = 18 valence electrons/T atom condition for the compound, *m*=1 electrons are expected to reside in In-based orbitals away from the Ir atoms. The void spaces in the structure provide a potential location for these states, in the rectangles of In atoms that bisect them (Figure 1a, gray plane). Thus, $IrIn_3$ in the $CoGa_3$ type is proposed to follow the 18-*n*+*m* scheme, with (*n*,*m*) = (1,1).

The situation is different for the low-temperature form of $IrIn_3$ (own type, space group *Pnma*). The structure features Ir atoms isolated from each other in layers of edge- and vertex-sharing Ir@In_9 tricapped trigonal prisms that lie in the *ac* plane (Figure 1b). The capping In atoms (indicated by dashed lines) also serve as the vertices of trigonal prisms in neighboring units. While these tricapped trigonal prisms are buffered by distorted In octahedra (yellow) that run in chains along the *b* axis, the structure lacks the wide void spaces of the $CoGa_3$ type, suggesting a denser packing arrangement. As the Ir atoms are too distant from each other for isolobal bond formation, *n* is expected to be 0. With 18-*n*+*m* = 18 for this compound, *m* should also be 0, nominally making this polymorph an (*n*,*m*) = (0,0) structure, in contrast to the (1,1) configuration of the $CoGa_3$-type form. The Ir atom, then, should attain an 18-electron configuration independent of other Ir atoms, and separate In-In bonding is not expected. This is consistent with an earlier quantum chemical study of the isoelectronic phase $IrIn_3$-type $IrGa_3$, where the electron localizability index (ELI-D) shows no direct Ga-Ga or Ir-Ir interactions but instead the prominence of 2-center and 3-center interactions involving Ir and Ga together.[19]

So far, this analysis has been based entirely on geometrical considerations. Adherence to the 18-*n*+*m* bonding scheme is often corroborated by a signature feature in the density of states (DOS): a band gap or pseudogap near the Fermi energy (E_F), analogous to a large HOMO-LUMO gap in molecular chemistry. The E_F of the DOS distribution for $CoGa_3$-type $IrIn_3$ meets this expectation (Figure 2). Notably, a band gap also appears approximately 0.5 eV below the E_F, corresponding to a 17-electron count, which explains the stability of 17-electron compounds, such as $FeGa_3$, $RuGa_3$, $OsGa_3$, $RuIn_3$, where (*n*,*m*) = (1,0).[22] For $IrIn_3$-type $IrIn_3$, however, the E_F is not so favorably placed in the DOS distribution; rather than lying within a clear DOS minimum, it falls to the electron-rich side of the nearest pseudogap (which correlates with a 17-valence electron count). While the $CoGa_3$-type form appears to be understandable in terms of an 18-*n*+*m* scheme, the relevance of this picture to the $IrIn_3$-type polymorph is not yet clear.

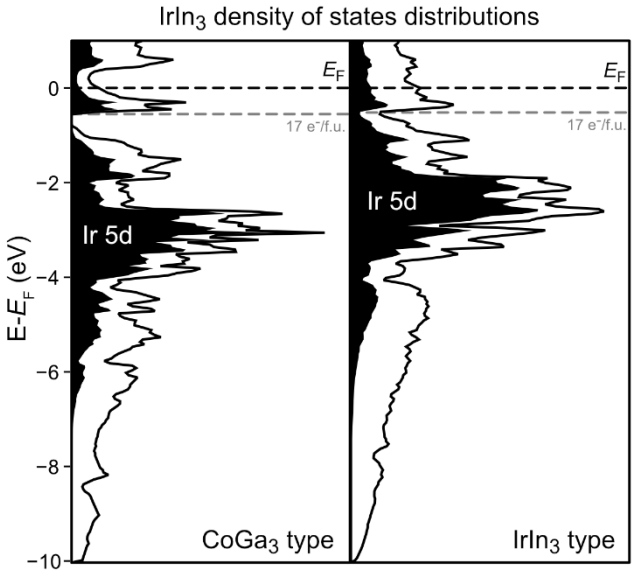

Figure 2. The electronic DOS distributions for $IrIn_3$ in the $CoGa_3$ and $IrIn_3$ structure types. The projected DOS contributions from Ir 5d states are filled in black. While the E_F (marked with a black dashed line) falls in a deep pseudogap for the $CoGa_3$-type system, the E_F for the $IrIn_3$-type is electron-rich relative to a pseudogap corresponding to 17 electrons/f.u. (gray dashed line).

The $IrIn_3$-type compound is not the first case where the DOS pseudogaps expected from the 18-*n* rule and structural connectivity are absent or misplaced. In a series of $REAl_3$ (*RE* = Sc, Y, lanthanides), the connectivity of the Ni_3Sn-type members appears to follow the 18-*n* rule, but the DOS distribution for this structure shows it is electron-deficient with respect to the nearest pseudogap.[40] DFT-raMO analysis revealed that Al-Al bonding states withdraw electrons from the *RE* atoms, raising the number of electrons needed for the 18-*n* electron configurations. Could a similar mechanism be at work here? To answer this question and test the proposed (*n*,*m*) assignments for the two $IrIn_3$ phases, we turn to DFT-raMO analysis.

3.2. DFT-raMO analysis of $CoGa_3$-type $IrIn_3$. Let's begin with the $CoGa_3$ type, as the pseudogap at its E_F is suggestive of a closed-shell electron configuration. The proposed 18-*n*+*m* configuration involves pairs of Ir atoms linked by an isolobal bond. Here, the electron pairs are associated with each of the Ir valence spd orbitals, with one of these belonging to an in-phase combination of orbitals from the two Ir atoms. Together this accounts for 17 electrons of the 18 electrons per Ir atom from the composition. The remaining electron is expected to reside in In-In bonding orbitals isolated from the Ir atoms, corresponding to the number *m*=1. The most likely location within the crystal structure for these In-based states is the squares of In atoms separating empty bicapped trigonal prisms (Figure 1a, gray plane).

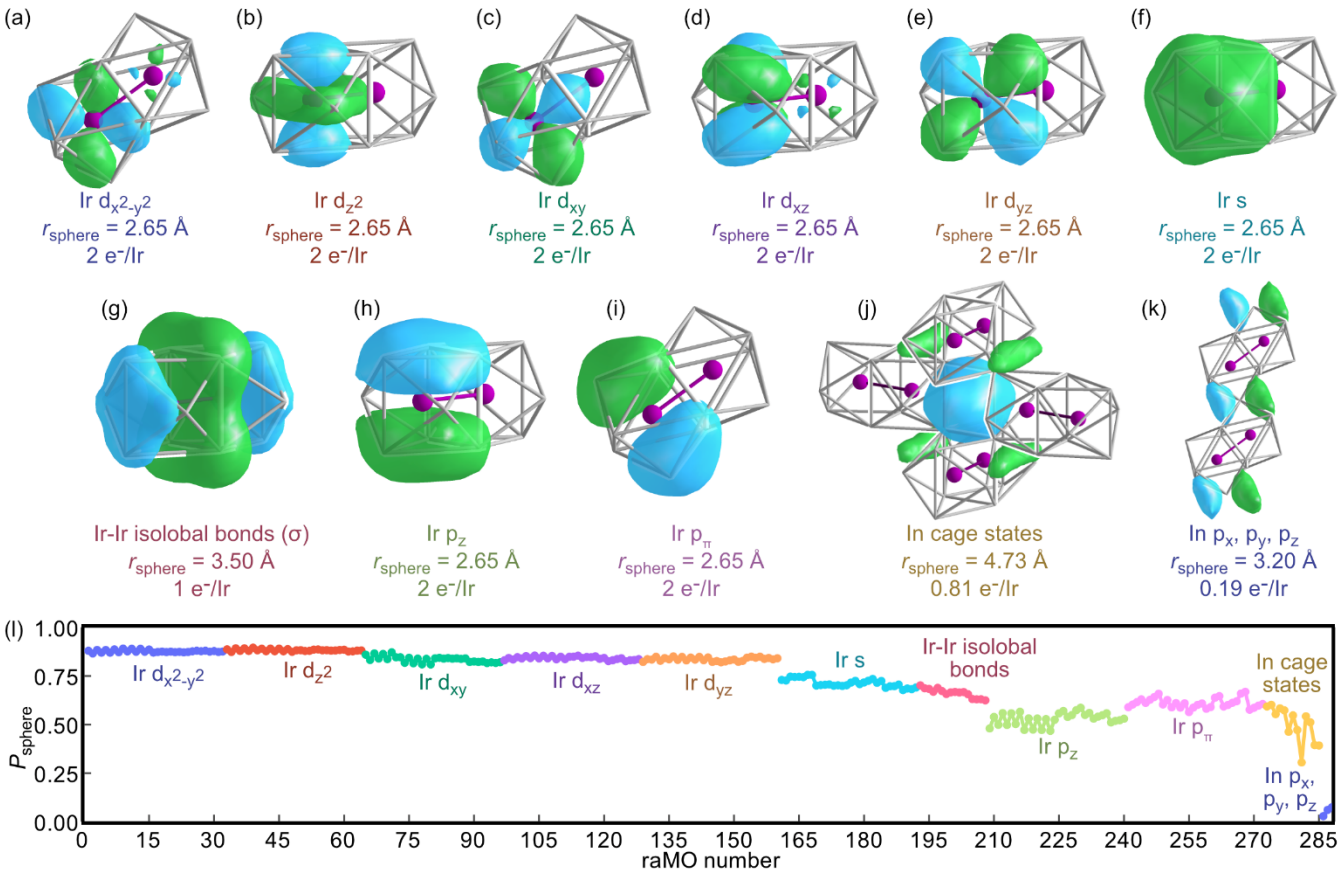

Figure 3. DFT-raMO scheme for $CoGa_3$-type $IrIn_3$, with isosurfaces of representative raMOs from each set of reconstructed states: (a-e) Ir 5d atomic orbitals, (f) Ir 6s atomic orbitals, (g) Ir-Ir isolobal bonds, (h, i) Ir 6p atomic orbitals, (j) In cage states, and (k) delocalized In 5p orbitals. (l) P_{sphere} values for each raMO, the fraction of each raMO's electrons localized within a sphere with radius r_{sphere} around the center of the target function.

To validate this hypothetical electronic scheme, we perform DFT-raMO analysis, a Wannier-type analysis that uses the occupied crystal orbitals as a basis set for the construction of molecular orbital-like targets based on Slater-type orbitals.[23] We begin our investigation by reconstructing the lower energy Ir 5d atomic orbitals, which are expected to be fully occupied. The orbitals are reconstructed in a serial fashion for the 32 Ir atoms within a 2×2×2 supercell. The quality of the reconstructed functions (raMOs) obtained from this sequence is monitored using the P_{sphere} metric, defined as the fraction of the raMOs electrons that lie within a fixed radius (r_{sphere}) of the target orbital's central point selected to encompass the first coordination sphere (unless otherwise stated).

The resulting raMOs show the expected d-like nodal character centered on the target Ir atoms (Figure 3a-e). Some functions, such as the d_{x2-y2} and d_{xz} raMOs show antibonding contributions from neighboring Ir atoms, likely an artifact of the orthogonality of the raMOs. Contributions of neighboring In atoms, combined with the right symmetry, are also evident. Across all five sets of 5d orbitals, the P_{sphere} values (r_{sphere} = 2.65 Å) show consistent and high degrees of localization (Figure 3l). As such, each Ir 5d orbital is considered filled with 2 valence electrons (32 raMOs × 2 electrons per raMO / 32 f.u.), for a total of 10 electrons per Ir atom.

Similarly, we reconstruct the Ir 6s atomic orbitals. Figure 3f shows a representative function nearly encompassing the entire bicapped trigonal prism. raMOs for all 32 Ir atoms in the supercell are constructed with the expected character and high P_{sphere} values. 2 electrons per Ir atom are assigned to the Ir 6s orbitals.

Next, we consider the Ir 6p orbitals. As the Ir-Ir dimer axes are rotated by 45° in the *ab* plane with respect to the crystal's axes, it is convenient to use a local coordinate system, defining the p orbitals as $6p_\sigma$, $6p_\pi$, and $6p_z$. Here, $6p_\sigma$ and $6p_\pi$ point along or perpendicular to the Ir-Ir contacts in the *ab* planes, respectively, while $6p_z$ is aligned with the *c*-axis. For the isolobal bonds, we reconstructed all 16 possible in-phase combinations of the $6p_\sigma$ orbitals on the pairs of Ir atoms. The isolobal functions show the expected σ-bonding character originating from the two Ir $6p_\sigma$ orbitals, as well as contributions from the square of nearest-neighbor In atoms that bridge the Ir-Ir contact to form the isolobal bond (Figure 3g). Across the sequence, the P_{sphere} values (r_{sphere} = 3.50 Å, twice the distance from the center of the Ir-Ir pair include for p-like character) are consistent, following the same trend as the 6s sequence before it. Thus, isolobal bonds are considered full, corresponding to 1 valence electron per Ir atom (16 raMOs × 2 electrons per raMO / 32 f.u.).

Finally, we move to the remaining Ir p orbitals, the Ir $6p_z$ and $6p_\pi$ orbitals. As all 32 raMOs for each 6p atomic orbital has consistent P_{sphere} values and the correct character (Figures 3h, i), the $6p_z$ and $6p_\pi$ orbitals are assigned 2 electrons/Ir atom each.

With this survey of the Ir atomic orbitals, we have accounted for 17 of the 18 valence electrons per formula unit in $CoGa_3$-type $IrIn_3$. This electronic configuration explains the 17-electron band gap lying 0.8 eV below the E_F (Figure 2) and the prevalence of 17-electron $CoGa_3$-type compounds. Such compounds would follow the 18-*n*+*m* scheme with an (*n*,*m*) configuration of (1,0).

$IrIn_3$, however, has one additional electron per Ir atom. As we outlined above, we anticipate that this 18th electron resides in bond-

ing interactions between In atoms that surround the structure's void spaces, where the Ir atoms are not expected to contribute to the bonding. For these targets, we constructed s-like functions situated in the centers of rectangles of In atoms surrounding open spaces (gray in Figure 1a). With the remaining states in the basis set, we successfully reconstructed raMOs for 13 of these 16 target functions. For this set of raMOs, the P_{sphere} values (with r_{sphere} = 4.73 Å, twice the distance from the center of the rectangle to its the In atom corners to include p-like features) are more scattered than the previous ones. However, the expected character of the raMOs is present in most of the functions (Figure S1a). Figure 3j shows one of these, with a large lobe sitting squarely in the center of four In atoms and p-like contributions coming from each of the In atoms.

Additional evidence for the residence of the 18th electron in these multicenter In cage states is provided by a selective application[48] of the Crystal Orbital Hamilton Population (COHP) analysis: in-phase overlap between In atoms across the diagonal of the rectangles is concentrated in the states just below the E_F (Figure S2). We thus assign electron pairs to 13 of the potential 16 In-In bonding functions, corresponding to 0.81 electrons per Ir atom.

The remaining three raMO functions (corresponding to 0.19 electrons/Ir atom) can be assigned by analyzing the remainder functions. These are distributed over the whole structure and appear to be constructed from linear combinations of p orbitals on the In atoms capping the Ir-centered trigonal prisms (Figure S1b). Accordingly, we attempt reconstruction of the three 5p orbitals of one of these In atoms. Figure 3k shows a fragment of the resulting raMO corresponding to the In $5p_y$ function. The function spreads out over the supercell (reflected by the low P_{sphere} value) but is concentrated on the capping In atoms linking trigonal prisms. Therefore, the last 0.19 electrons/Ir atom are allocated to In 5p orbitals.

In summary, DFT-raMO analysis of $CoGa_3$-type $IrIn_3$ uncovers how the Ir atom nearly achieves a closed-shell electronic configuration. 16 valence electrons populate to the atomic orbitals of Ir ($6s^2$ $5d^{10}$ $6p^4$). σ isolobal bonds are then formed from the combination of p_σ orbitals between neighboring Ir atoms, with bonding contribution from the nearby In atoms. The last valence electron resides in multicenter In-based states between trigonal prism units, with the In 5p orbitals taking a fraction of these electrons (explaining why the DOS shows a pseudogap rather than a band gap at the E_F). This corresponds to an 18-n+m configuration, with (n,m) = (1,1).

3.3. DFT-raMO analysis of $IrIn_3$-type $IrIn_3$. Based on our earlier geometrical analysis and the DOS distributions, we expect the bonding scheme for the other $IrIn_3$ polymorph, in its own structure type, should be different. DFT-raMO analysis explains how. We begin by reconstructing the Ir spd valence orbitals toward the creation of filled 18-electron configurations, starting from the ones most contracted around the nuclei: the Ir 5d atomic orbitals. The P_{sphere} values (r_{sphere} = 2.90 Å) for this sequence of raMOs are consistently high (Figure 4k), while the raMO functions show the expected centering on the Ir sites, as well as bonding contributions from neighboring In atoms (Figure 4a-e). These results confirm the complete occupation of the d subshell; 10 of the 18 valence electrons per Ir atom are associated with the Ir 5d orbitals.

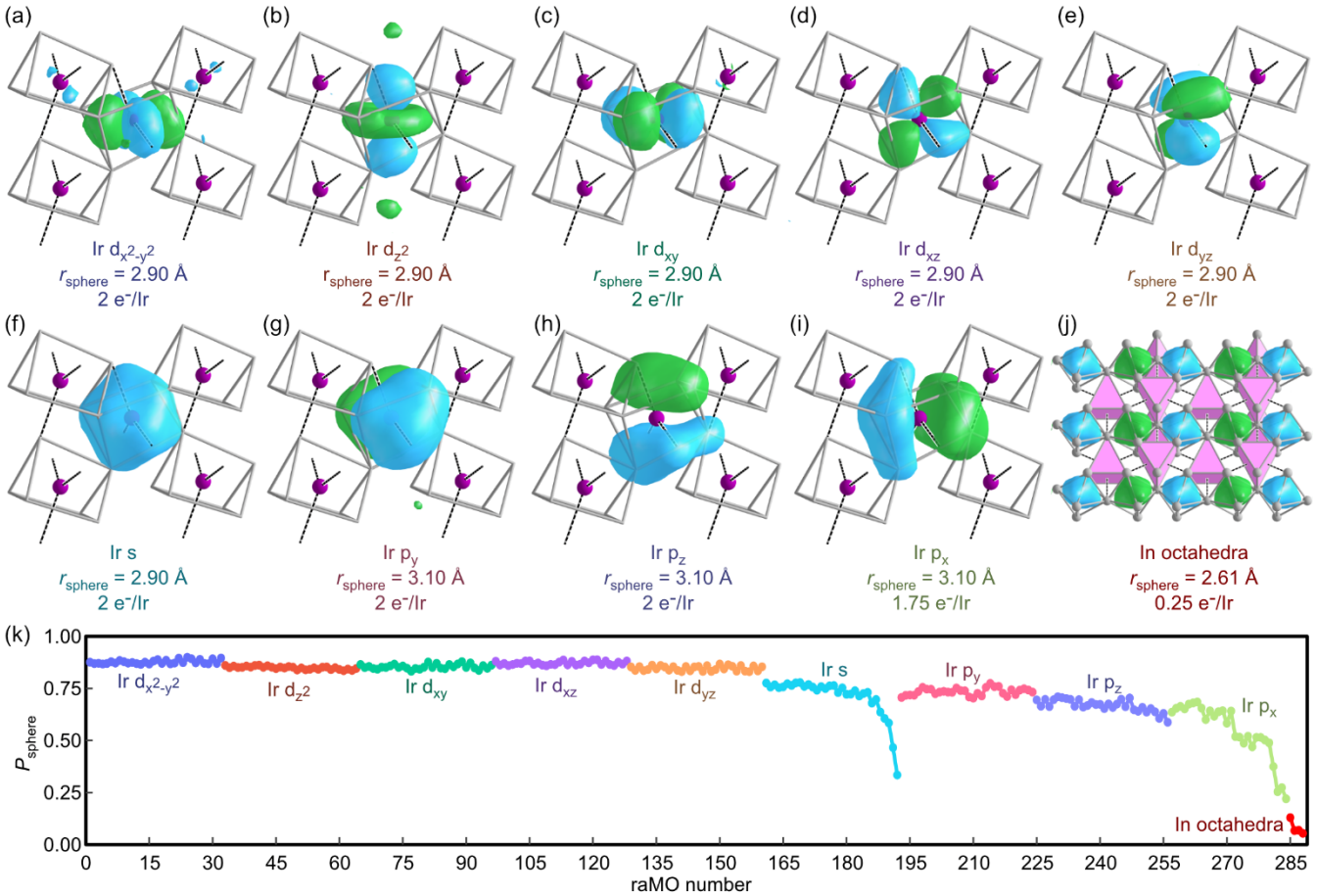

Figure 4. DFT-raMO scheme for $IrIn_3$-type $IrIn_3$. Isosurfaces of representative raMOs from each set of reconstructed local orbitals: (a-e) Ir 5d atomic orbitals, (f) Ir 6s atomic orbitals, (g-i) Ir 6p atomic orbitals, and (j) delocalized states concentrated in In octahedra. (k) P_{sphere} values across the sequence of DFT-raMO reconstructions.

Next, we construct the Ir 6s atomic orbitals. The resulting raMOs nearly cover the entire tri-capped trigonal prism suggesting substantial Ir-In interactions (Figure 4f). P_{sphere} is consistent for most of this sequence but drops sharply for the last 2 of the 32 functions. Inspection of these last two raMOs shows the expected s-like character (Figure S3) but greater delocalization, likely from the reduction of available functions in the basis set due to the generation of the previous raMOs. In addition, if we reject these two functions, remainder functions with Ir s character appear later in the analysis. As such, we allocate 2 electrons to each of the Ir 6s atomic orbitals, corresponding to 2 electrons/Ir atom.

The reconstructions of the Ir $6p_z$, $6p_y$, and $6p_x$ proceed in an analogous way, except the P_{sphere} values for the $6p_x$ raMO functions decrease near the end of the sequence. In this case, p_x character is maintained (Figure S4) until the last 4 of 32 possible raMO functions, where P_{sphere} drops precipitously. The final attempts to create $6p_x$-based raMOs lead to functions with no such character (Figure S5). Only 5.75 of the expected 6 electrons per Ir atom are then associated with Ir 6p orbitals.

So far, we have accounted for 17.75 electrons of the 18 per Ir atom as occupied Ir-based functions. Where are the last 0.25 electrons? Hints can be found in the discarded raMOs from the Ir $6p_x$ sequence: these contain s-like lobes centered on distorted octahedral interstitial spaces surrounded by In atoms (Figure S5). This suggests that the remaining electrons occupy In octahedral cage states. With this new hypothesis, we attempt to reconstruct s-like functions centered in the distorted In octahedra. P_{sphere} values (r_{sphere} = 2.61 Å, selected to encompass density within the targeted In octahedra) for the whole set of raMOs are low as the functions are delocalized in chains along the *b* axis (Figure 4j). However, inspection of the isosurfaces display the expected character. The last 0.25 electrons are then assigned to the In octahedra.

How should we make sense of this electronic scheme? In a classic 18-electron configuration, the s, p, and d orbitals of the transition metal are all associated with electron pairs. In $IrIn_3$-type $IrIn_3$, however, the occupancy of the Ir $6p_x$-based raMOs is partially depleted by electron transfer to the In octahedra. This phenomena of main group-based crystal orbitals crossing below other bands has been observed in other T-E intermetallics.[40]

The depopulation of the $6p_x$ orbitals does, however, come with an advantage. Recall that the tri-capped trigonal prism units form chains along the *a*-axis. This sets up the $6p_x$ orbitals of neighboring Ir atoms in the chain to overlap, with the potential of forming a band that spans from σ- to σ*-like interactions. The reduced population of the $6p_x$ orbitals corresponds to the removal of electrons from the top of this band, leading to net Ir-Ir bonding character. Indeed, the pseudogap at 17 electrons in the DOS for $IrIn_3$-type $IrIn_3$ corresponds to the half-filling of this $6p_x$ set of functions, where the p_x-p_x bond order would be maximized.

We are now ready to compare how the two polymorphs of $IrIn_3$ relate to the 18-*n*+*m* scheme. The geometry of the $CoGa_3$ phase, through Ir-Ir pairs and open spaces in the structure, permits the formation of isolobal bonds between Ir atoms and multicenter In-In bonds, leading to the (*n*,*m*) configuration (1,1). The structure of the $IrIn_3$ phase, on the other hand, accommodates its electrons in a different manner. The near-completion of independent 18-electron configurations on the Ir atoms suggests an (*n*,*m*) scheme of (0,0). However, there is some electron transfer from highest energy of the Ir $6p_x$-based orbitals to low-lying cage states based in In octahedra, leading to the configuration (*n*,*m*) = (0.25,0.25).

From these results, one may gain the sense that the $CoGa_3$ type is more electron-precise and would thus be favored from the viewpoint of electronic stability. This conclusion is affirmed by the deep pseudogap at the E_F in its electronic structure. However, experimentally, the low-temperature phase is in fact the $IrIn_3$-type polymorph, suggesting that this later structure has a lower energy. In the next section, we will trace the unexpected stability of the $IrIn_3$ type to packing effects with DFT-Chemical Pressure analysis.

3.4. Global and Local Packing Factors. In the previous section, we saw that electronic considerations alone were not sufficient to explain the relative stabilities of the $CoGa_3$-type and $IrIn_3$-type forms of $IrIn_3$. Another factor apparently plays a larger role in structural preference. When comparing the two structures, one difference stands out: their packing efficiency. The $CoGa_3$ type has large pockets of open space, while the $IrIn_3$ type appears to be more densely arranged. The consequences of these packings can be analyzed with the DFT-Chemical Pressure (CP) method. In this method, the output of DFT calculations is used to generate maps of the energetic response of a structure to expansion and contraction. The result is a pressure distribution for the structure interpretable in terms of interatomic pressures, which can be projected onto atom-centered spherical harmonics for visualization. As these local pressures represent stresses arising from the packing constraints of a structure (as opposed to an external force) we refer to them as *chemical pressures.*

Let's begin with the CP scheme of $CoGa_3$-type $IrIn_3$. In Figure 5a, CP features are overlaid on a single layer in the *ab* plane of the structure. In this scheme, each atom is shown with radial distribution of lobes corresponding to the pressure magnitudes it experiences along each direction. The signs of the pressures are indicated with color: white lobes represent positive CP along interatomic contacts, where atoms are packed too closely, and expansion is favored. Conversely, black lobes indicate negative CPs where interatomic contacts are overextended and would prefer contraction.

The CP scheme in Figure 5a reveals packing tensions within the $CoGa_3$-type structure. The CP features for the Ir atoms are dominated by positive CPs (white lobes). These are directed toward their In neighbors, which show complementary positive CPs pointing back at the Ir atoms. The predominance of positive CP on the Ir atoms is indicative of an overly constricted coordination environment. However, expansion of the structure to relieve this tight packing is opposed by negative pressures (black lobes) along the In-In contacts (as well as, to a lesser degree, negative CP along the Ir-Ir dumbbell axes). The In-In interactions are already overly stretched and resist the expansion called for by the Ir-In interactions. This tension between forces for expansion and contraction is particularly striking in the pairs of bicapped trigonal prisms that host the Ir dimers: positive pressures exist between the Ir atoms and their In neighbors, while negative pressures run along the In-In contacts that surround the Ir dumbbells.

Looking beyond the local environments of the Ir atoms, their arrangement in space relative to each other also gives rise to longer-range packing tensions. The Ir-In positive CPs trace parallel paths between trigonal prism units along the Ir atoms and capping In atoms (Figure 5a, red). These paths of positive pressure are perpendicular to paths of negative pressure, which run between the capping In atoms and the void spaces (blue), seemingly allowing a

path for the structure to relax. However, these features in neighboring *ab* layers are rotated by 90° along the *c* axis, creating a 3D framework of positive CP. As a result, any contraction of the structure along the *ab* plane to relieve negative pressures would run directly in conflict with the positives pressures in neighboring *ab* layers (Figure S6). It appears, then, that the paths of positive pressures hold open the void spaces between the filled units, which in turn induces further packing strain, as indicated by negative pressures pointing toward the voids.

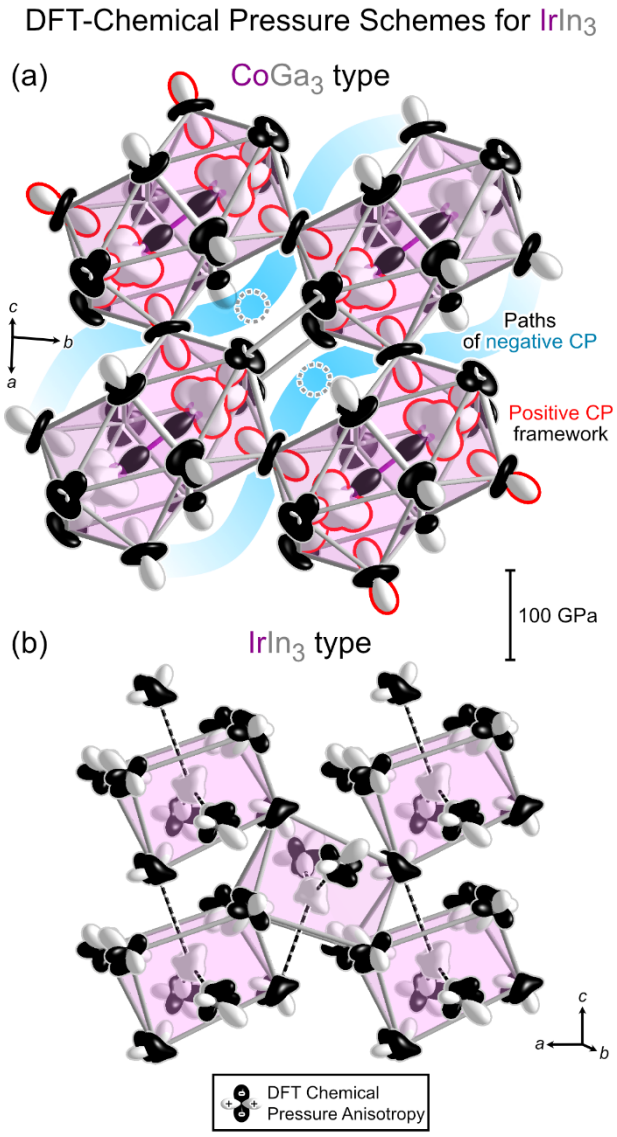

Figure 5. DFT-Chemical Pressure schemes for $IrIn_3$ in the (a) $CoGa_3$ and (b) $IrIn_3$ types. White lobes between atoms represent positive pressure where interatomic contacts are overly contracted, while black lobes denote negative pressure where contacts are overly extended.

How does this compare to the CP scheme of the $IrIn_3$-type polymorph? The CP scheme of $IrIn_3$-type $IrIn_3$ is shown in Figure 5b. As in the $CoGa_3$ structure, the Ir atoms exhibit positive pressures pointing outward to the In atoms that form the tricapped trigonal prismatic arrangement. These positive pressures are mostly isotropic except for a decrease in the pressure between Ir atom and the capping In atom in the same *ac* plane. Negative pressures along In-In contacts persist, indicating these contacts are also overly extended in this structure type. However, comparison of the $CoGa_3$ and $IrIn_3$ CP schemes show decreased magnitudes of the CP features in the $IrIn_3$-type relative to the $CoGa_3$ type, indicating reduction of packing stress at these contacts. This can be connected to the observation that these networks of positive CPs are not required to hold open such large void spaces as those in the $CoGa_3$ type.

Using these CP schemes, we can predict how changes in the relative sizes of the T or E atoms influence the packing tensions. The $CoGa_3$-type CP scheme features positive CPs mainly on the T atoms, and negative pressures toward void spaces on the E atoms. As such, we can predict that reducing the size of the T atom (or increasing the size of the E atom) will relieve the chemical pressures present in the $CoGa_3$ structure type. While the same would apply to the $IrIn_3$ type, the extent of this relief should not be as pronounced, as the packing tensions in this structure are less intense. Indeed, $CoIn_3$ (T-E radius-ratio r_T/r_E = 0.753) forms exclusively in the $CoGa_3$-type,[17] while $IrGa_3$ (r_T/r_E = 0.962), like $IrIn_3$ (r_T/r_E = 0.816), has both a low-temperature $IrIn_3$-type phase and a high-temperature $CoGa_3$-type phase.[19]

To examine how the radius-ratio influences these structural preferences, we extended our CP analysis to both $CoIn_3$ and $IrGa_3$ in these structure types. We begin at the top of Figure 6 with both compounds in the $CoGa_3$ type. The CP scheme of $CoIn_3$ (Figure 6a) is like that of $IrIn_3$ (Figure 5a) with one key difference: the shape of the negative CP lobe on the In atoms capping the trigonal prisms is different. In $CoGa_3$-type $IrIn_3$, this CP lobe assumes a ring-like shape, but now, in $CoIn_3$, this feature is heavily reduced and mainly points along the *c* direction. As such, this In atom in $CoIn_3$ experiences little negative pressure towards the void space. The smaller size of the Co atoms allows the trigonal prismatic units to contract, which invites the In-In contacts to shorten. The volume associated with the void spaces is then reduced, leading to less negative CPs in the structure.

The analogous atom in the CP scheme of $IrGa_3$ in the $CoGa_3$-type shows the opposite effect (Figure 6b). The ring of negative pressures on this Ga atom is stretched in the direction of the empty void. This is simply understood from the large r_T/r_E ratio of 0.962. If we begin with $IrIn_3$ and replace the In atoms with smaller Ga atoms, the Ga atoms then experience greater negative CPs towards the empty spaces. This further supports the notion that the packing stresses associated with these void spaces correlate with the stability of the $CoGa_3$-type structure.

Does the $IrIn_3$ structure type offer reduced packing tensions to $CoIn_3$ and $IrGa_3$ in the same way that it does for $IrIn_3$? The CP schemes for $IrIn_3$-type $CoIn_3$ and $IrGa_3$ yield different answers to this question. The CP scheme for $IrIn_3$-type $IrGa_3$ (Figure 6d) is quite like that of $IrIn_3$ (Figure 5b): the Ir atoms display largely isotropic positive CPs directed towards their neighboring Ga atoms, while negative CPs run along the Ga network. In addition, the CP magnitudes are reduced relative to those in $CoGa_3$-type form of $IrGa_3$ (Figure 6b). $IrGa_3$ with its two polymorphs, then, largely follows the same packing trends as $IrIn_3$.

The $IrIn_3$-type $CoIn_3$ scheme, however, shows different features (Figure 6c) than those of the other examples. Most noticeably, the chemical pressures on each Co atom are more anisotropic. While eight of the nine Co-In contacts around it experience positive CP, a sizeable negative CP lobe present on the Co atom points to the ninth In neighbor, a capping In atom lying in the same *ac* plane. The Co atom is, in fact, off-center in the trigonal prism, leaning towards this capping atom; however, further shortening of this Co-In contact is prevented by collisions with large positive CPs from

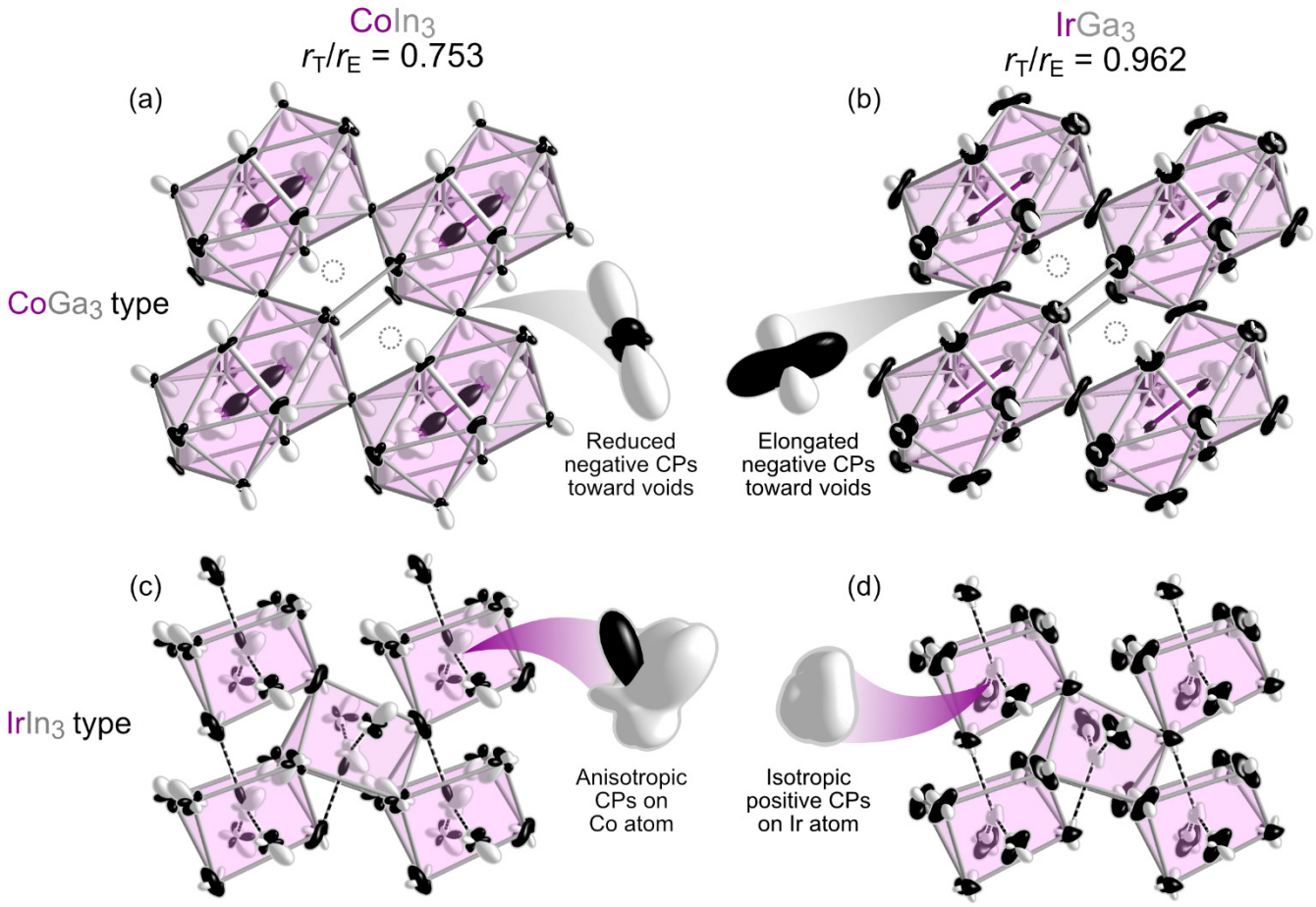

Figure 6. CP schemes of $CoIn_3$ and $IrGa_3$ in the (a, b) $CoGa_3$ and (c, d) $IrIn_3$ structure types, showing the effect of the T-E radius ratio on the atomic packing tensions. The negative CPs on the main group atom pointing towards void spaces of the $CoGa_3$ type are reduced in $CoIn_3$ but are enlarged in $IrGa_3$. CPs experienced by the T atoms in the $IrIn_3$ type are relatively isotropic for $IrGa_3$, but the emergence of anisotropic features on the analogous Co atom in $CoIn_3$ suggests that the Co is a poor fit for this environment.

the other In atoms making up the trigonal prism. Put simply, the Co atom is small enough that the In atoms crowd each other out as they interact with it.

From this, we can observe the role r_T/r_E plays in atomic packing in these systems. The $CoGa_3$-type structure inherently has packing stress, with extended paths of positive CPs holding open void spaces that generate negative CPs. A lower r_T/r_E value (such as in $CoIn_3$) can reduce this stress as this gives smaller capped trigonal prism units relative to the preferred E-E distances around the voids. With higher r_T/r_E values (such as in $IrGa_3$), the opposite occurs: bigger T atoms require a larger capped trigonal prism unit, and smaller E atoms experience more negative pressure toward the open spaces, exacerbating the packing issues.

The $IrIn_3$-type structure, however, offers a preferrable alternative, in some cases. For high r_T/r_E values, the absence of large void spaces, which call for the contraction of the structure, leads to lower positive CPs on the T atoms. For $IrGa_3$ and $IrIn_3$, this effect is strong enough that the $IrIn_3$ type is energetically favored, despite its DOS distribution showing weaker electronic stability. For smaller T atoms, though, the coordination environment in $IrIn_3$-type can lead to some Ir-In interactions being under-utilized, as shown by the Co-In contact with negative CP in Figure 6c. It is understandable then that no $IrIn_3$-type form of $CoIn_3$ has yet been discovered.

3.5. Chemical Pressure Quadrupoles: Links to Vibrational Entropy and Phase Transitions. Up until now, we have focused on the role of energy in the relative stabilities of the $IrIn_3$ polymorphs. These considerations suffice for making predictions at T = 0 K. However, when exploring the potential of a phase transition at higher temperatures, the role of entropy comes to the foreground. As lattice vibrations are the primary source of temperature-dependent entropy in crystals (barring configurational entropy),[49] the possibility of a phase transition between these two structures relates to differences in their phonon band structures.

As we showed previously,[50] the DFT-CP approach can be used as a guide to the relative frequencies and characters of phonon models. One of the most significant motifs to arise in CP schemes, the quadrupole, features positive and negative pressures oriented perpendicularly to each other, creating d-orbital-like distributions.[51] Such motifs are familiar from our analysis of the $CoGa_3$ type. The CP lobes on the E atoms capping the T-centered trigonal prisms define a d_{z2}-shaped arrangement (Figures 5a, 6a,b), with positive pressures pointing towards T atoms and a perpendicular ring of negative pressures pointing into the void spaces.

In such situations, the directions of the negative and positive pressures of the quadrupoles correlate with directions of soft and hard atomic motion, respectively.[50] As negative CPs reflect interatomic contacts that are overly long, atomic motion that shortens those contacts (while lengthening other contacts with positive CP) will encounter little resistance. Consequently, atomic motions along the direction of negative features of CP quadrupoles tend to contribute to low frequency phonon modes. The reverse is also

true: movements that compress contacts experiencing positive CP will face a higher energetic cost and will thus contribute to higher frequency modes. For the case of $CoGa_3$-type $IrIn_3$, we can predict that phonons involving the capping In atom will be low frequency when the motions are perpendicular to the Ir-In-Ir axis they lie within, while motions along these axes will be stiffer, particularly when the Ir atoms are moving in an out-of-phase manner relative to the capping In atom between them.

The quadrupolar character of an atom can be quantified with the quadrupole metric (QP):[51]

$$\mathrm{QP} = \frac{\left(\sum_m c_{l=2,m}^2\right)}{\sum_{l=0}^{l_{\max}=4}\left(\sum_m c_{l,m}^2\right)} \qquad (1)$$

where the $c_{l,m}$ coefficients refer to the contributions of the Y_{lm} spherical harmonics to the angular CP distribution around the atom:

$$\mathrm{CP}(\theta,\varphi) = \sum_{l\le l_{\max}}\left(\sum_{-l\le m\le l} c_{l,m}Y_{l,m}(\theta,\varphi)\right) \qquad (2)$$

A CP feature with QP=0 refers to a site with no contributions from l=2 spherical harmonics, while QP=1 describes a distribution entirely built from such functions, perfectly resembling a d-orbital in its angular dependence.

The QP values for CP features in $CoGa_3$- and $IrIn_3$-type $IrIn_3$ are tabulated in Table 1. QPs for the Ir atom sites are relatively low for both phases (<0.1), which aligns with their overwhelmingly positive CPs. The QP values for the In sites in $CoGa_3$-type $IrIn_3$ are 0.959 and 0.659 for the In atoms capping and constituting the trigonal prisms, respectively. By contrast, the QP values for the In atoms in $IrIn_3$ are both below 0.50. The In atoms, then, find much higher quadrupolar character in the $CoGa_3$-type structure. This is expected to translate to the presence of low frequency modes for the $CoGa_3$ type.

Table 1. Chemical Pressure Quadrupole (QP) Metric Values for the Polymorphs of $IrIn_3$ (l_{max} = 4)

Element	$CoGa_3$-type	$IrIn_3$-type
Ir	0.068	0.048
In	0.959	0.490
	0.695	0.483

These predictions are confirmed by phonon band structures obtained from LDA-Density Functional Perturbation Theory (DFPT) calculations. Figure 7a shows the phonon dispersion curve and phonon density of states of $CoGa_3$-type $IrIn_3$. The frequencies of the optical modes span from about 0.7 THz to 6.8 THz, with a band gap between 4.4 THz to 5.2 THz, drawing a clear distinction between sets of low and high frequency modes. Whereas the Ir atoms, with their heavier mass, would normally be expected to dominate the low frequency side of this distribution, the Ir projected DOS (shaded in black) shows that they do not contribute significantly below 2 THz. Instead, the lowest frequency modes are based on motions of the In atoms, despite their lighter atomic mass. This is in line with the prominence of CP quadrupole character on the In atoms.

Inspection of the phonon modes affirms this conclusion. As an example, the lowest frequency optical mode at the Γ-point is plotted in Figure 7b, with yellow arrows showing directionality of atomic movement and CP features given for a selection of atoms. The largest motion in this mode is indeed the movement of the capping

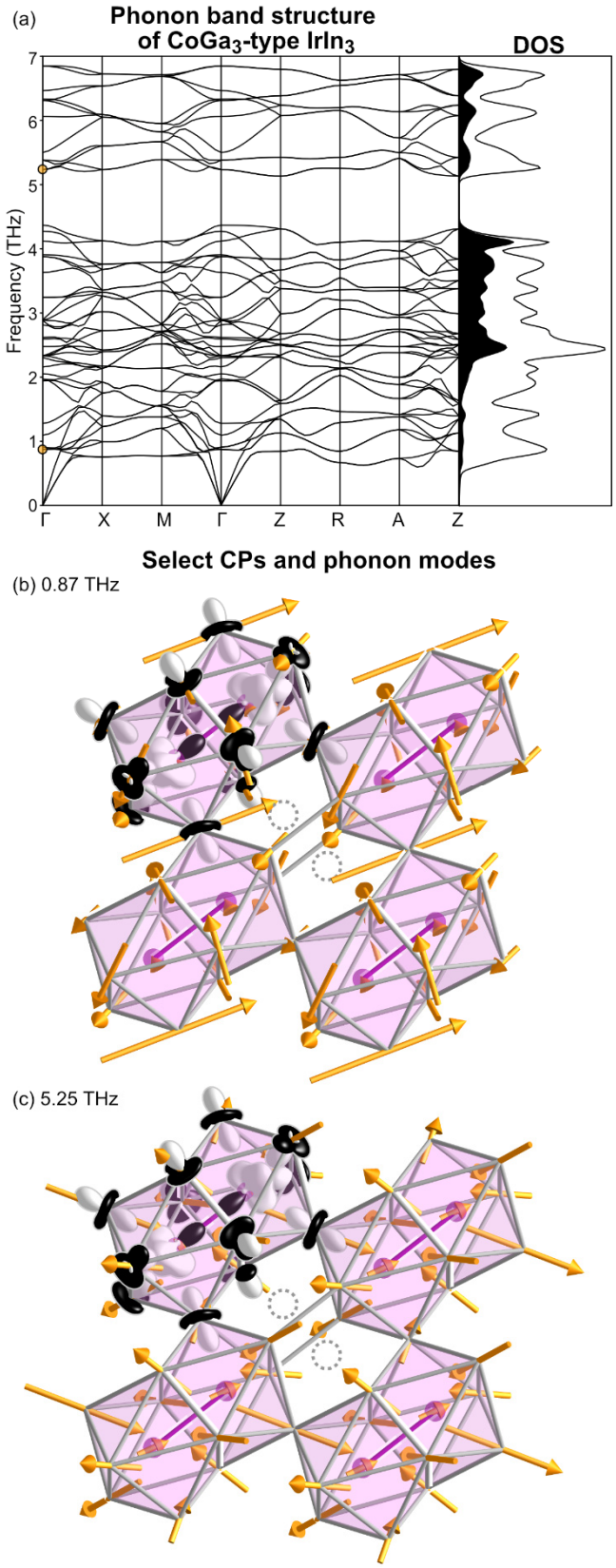

Figure 7. Connections between the phonon band structure and CP quadrupoles in $CoGa_3$-type $IrIn_3$. (a) The LDA-DFT phonon band structure and phonon density of states (DOS) distribution, with contributions from the Ir atom to the DOS shaded in black. Orange dots on the dispersion curve mark the frequencies of selected phonon modes, which are (b,c) plotted over a partial CP scheme of $CoGa_3$-type $IrIn_3$.

In atoms into and out of the neighboring void spaces, following paths of negative CP. Smaller arrows on the In atoms of the trigonal prisms correspond to a distortion of the trigonal prismatic units along the negative components of their CP quadrupoles.

The expectations regarding CP quadrupoles also hold true for the high frequency modes. No motion involving contraction along the positive CP components of the quadrupoles is observed at Γ until 5.25 THz, just above the band gap. In Figure 7c, arrows show the motions for this mode. Here, the Ir atoms collide with the trigonal prism edges directly along their axes, leading to contraction of Ir-In contacts with positive CP. Additionally, motions along the positive features of the quadrupole are apparent. Inspection of other modes in the upper bands show other contraction/stretching motions of other contacts with positive CP.

Such a dichotomy between high and low frequency phonons is absent in the $IrIn_3$ type. The $IrIn_3$ phase has lower QP values, suggesting that any paths of soft motion are less distinct. This is confirmed by the calculated phonon dispersion curve and density of states of the $IrIn_3$ type (Figure 8). The lowest optical mode at the Γ-point now appears at a frequency of 1.40 THz, compared to 0.87 THz for the $CoGa_3$ type. Additionally, the lower spread separating high and low frequency modes is consistent with the lowered quadrupolar character.

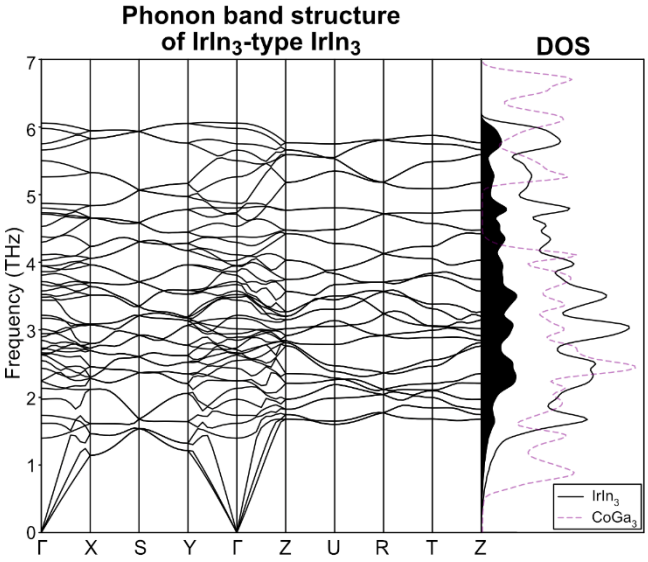

Figure 8. LDA-DFT phonon band structure and phonon DOS distribution of $IrIn_3$-type $IrIn_3$. The phonon DOS of $CoGa_3$-type $IrIn_3$ is shown with a light purple dotted curve for comparison.

Let's now consider how these differences in the phonon modes influence the stability of the polymorphs. The vibrational entropy, S_{vib}, at temperature T arising from the phonon modes for a crystal containing 3N atoms is given by[49]

$$S_{\mathrm{vib}}(\mathrm{T}) = k_{\mathrm{B}} \sum_{i}^{3N} \left[-\ln\left(1 - e^{\frac{-\varepsilon_i}{k_{\mathrm{B}}T}}\right) + \frac{\frac{\varepsilon_i}{k_{\mathrm{B}}T}}{e^{\frac{\varepsilon_i}{k_{\mathrm{B}}T}} - 1} \right], \quad (3)$$

where k_{B} is the Boltzmann constant, and ε_i is the energy eigenvalues for normal mode *i*. According to this relationship, lower frequency modes generally contribute more entropy per mode at any given temperature than the higher frequency modes.

This is visualized in Figure 9a, where we plot the phonon DOS for the $CoGa_3$-type again, this time with the modes weighted by their relative entropic contributions at two temperatures, T = 100 K (blue) and 700 K (red). In both cases, the contributions to S_{vib} for the lower frequency modes are higher relative to the DOS values. In this way, the presence of softer phonon modes in the $CoGa_3$ type than the $IrIn_3$ type leads to it having a higher S_{vib} value for a wide range of temperatures.

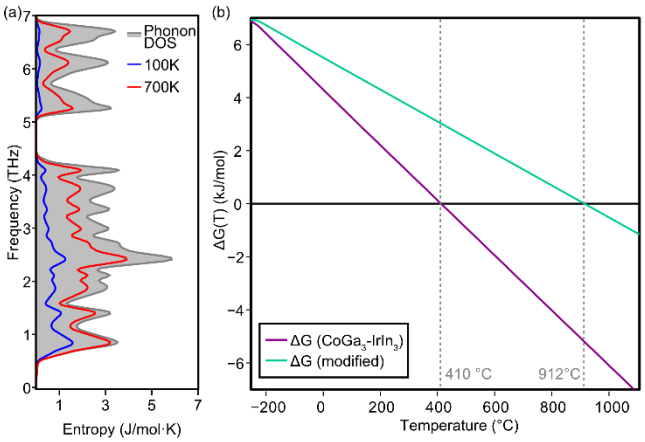

Figure 9. Phonon contributions to vibrational entropy. (a) Relative entropic contributions of the phonon modes to the total vibrational entropy of $CoGa_3$-type $IrIn_3$ at 100 K (blue) and 700 K (red). The phonon DOS (gray) is shown for comparison but is not to scale with the entropy curves. (b) The difference in free energy between the $CoGa_3$ and $IrIn_3$ type polymorphs as a function of temperature. ΔG = 0 at 410°C (purple). When the lowest frequencies in the phonon DOS distribution of $CoGa_3$ are increased by 0.53 THz, the calculated phase transition temperature rises to 912°C (green).

From these considerations, we can estimate the Gibbs free energy change, ΔG, for the $IrIn_3$ type to $CoGa_3$ type transition as a function of T, with the goal of predicting the transition temperature. For a system at P=0 GPa, ΔG = ΔE-TΔS, where in this case ΔE is positive (reflecting the better packing efficiency of the $IrIn_3$ type for the compound $IrIn_3$) and ΔS is positive (consistent with the $CoGa_3$ type's greater vibrational freedom). In Figure 9b, we plot in purple the ΔG(T) derived from the T=0 K energy difference and the ΔS(T) values obtained from the phonon band structure. As expected from ΔE > 0 and ΔS > 0, the curve begins at positive ΔG values at T = 0 K, and slopes downward, crossing zero at approximately 410°C. This represents the predicted transition temperature, and is in fair agreement with the experimentally estimated value of 350°C. This analysis could be enhanced with corrections to the harmonic approximation and inclusion of other environmental and entropic effects.[49,52] However, a simple evaluation of the phonon frequencies appears to capture the essence of the driving force for the transition.

To what extent does this transition connect to the CP quadrupole-induced softening of the lowest frequency optical modes? We explore this by artificially suppressing the lowest peak in the phonon DOS for the $CoGa_3$ type and recalculating the vibrational entropy and the phase transition temperature. As an example, we considered the case when the vibrational frequencies contributing to the lowest frequency peak in the $IrIn_3$-type $IrIn_3$ phonon DOS (those below 1.21 THz) were increased by 0.53 THz, corresponding to the difference in frequency between the two polymorphs' lowest optical modes. The resulting decrease to S_{vib} raises the phase transition temperature to 912°C (green curve in Figure 9b). This jump of 502°C demonstrates the key role the softened phonon

frequencies play to the high temperature stability of the $CoGa_3$ type.

In summary, the combination of CP schemes and the phonon band structures reveals the structural origins of the $CoGa_3$ type's emergence as a high-temperature form of $IrIn_3$. Its strong CP quadrupolar features, created by the presence of void spaces in the structure, lead to softer phonons modes than those in the competing $IrIn_3$ type. This provides the $CoGa_3$ type with a larger vibrational entropy, making this structure increasingly favored as the temperature is raised.

4. CONCLUSIONS

In this Article, we have uncovered the factors underlying polymorphism in $IrIn_3$. DFT-raMO analysis reveals that the electronic configurations of both phases relate to the 18-*n* rule, following 18-*n*+*m* bonding schemes with different (*n*,*m*) configurations. The (1,1) configuration of the $CoGa_3$ type provides clearer electronic stability in the form of a deep pseudogap at the E_F. However, the role of electronic stability is overshadowed by atomic packing effects, as demonstrated with DFT-CP analysis. The electronically favored $CoGa_3$ type possesses large void spaces, which are held open by lattices of positive CPs in the network of Ir-In contacts. The $IrIn_3$ type provides a more efficiently packed alternative, which is expected to be preferred for larger r_T/r_E ratios. The $IrIn_3$ type has less empty space, minimizing local stress by allowing the packing environment of the Ir atoms to expand. However, at higher temperatures the more open $CoGa_3$-type gains favorability due to its higher vibrational entropy.

From this picture, we can understand the broader trends over the family of related 18-electron compounds adopting one or more of these structure types. In Figure 10, we show a structure map in which the lowest energy structure type of each TE_3 composition is plotted as a function of the sum of T and E radii and the r_T/r_E radius-ratio. For compounds labeled in red, the lowest energy phase is the $CoGa_3$ type, while compounds labeled in blue correspond to the $IrIn_3$ type as the lowest energy phase from LDA-DFT calculations. Two lines emerge, corresponding to E = In and E = Ga series. Only $IrIn_3$ and $IrGa_3$ preferentially form the $IrIn_3$ type, which is consistent with their having the highest r_T/r_E ratios within their series.[16,19] Though $RhIn_3$[17] and $RhGa_3$[21] have only been observed in the $CoGa_3$ type, the energy differences are relatively low (see Supporting Information), suggesting that $IrIn_3$-type polymorphs may be accessible through other synthetic routes such as high-pressure synthesis.

CP analysis and the 18-*n*+*m* bonding scheme can also be used to rationalize substitutional patterns in ternary variants of the $CoGa_3$ types. In the solid solutions of $IrIn_{3-x}Mg_x$[53], $CoIn_{3-x}Zn_x$, and $CoGa_{3-x}Zn_x$,[54] the smaller Zn or Mg atoms preferentially substitute onto the capping E atom site as opposed to the sites composing the vertices of the trigonal prisms. This matches with trends observed in the CP schemes of the $CoGa_3$-type: the CP features of the former atoms show less overall negative pressure than the latter atoms (see the Supporting Information). In another example, the 16-electron $CoGa_3$-type $ReGa_3$ only exists as a high-pressure phase; however, substitution of Ga with Ge pushes the E_F into a pseudogap, leading to the 17-electron $ReGa_2Ge$ ternary phase being stable at ambient conditions.[55,56]

This analysis of polymorphism in the $IrIn_3$ system opens avenues to investigating a more general phenomenon in T-E intermetallics, 18-*n*+*m* isomerism, where the availability of multiple structures with different (*n*,*m*) configurations exist for any given electron count. In $IrIn_3$, the existence of two 18-*n*+*m* isomers emerges from the conflict between prioritizing packing efficiency ($IrIn_3$ type, *n*=*m*=0.25) or vibrational entropy ($CoGa_3$ type, *n*=*m*=*1*), which is supplemented by differences in electronic stability. A preliminary search of the Inorganic Crystal Structure Database[57] has uncovered numerous binary structure types adopted by T-E intermetallics which can be combined into series of 18-*n*+*m* isomers. We are looking forward to investigating these situations in search of general principles for how atomic packing and vibrational properties correlate with combinations of *n* and *m* values.

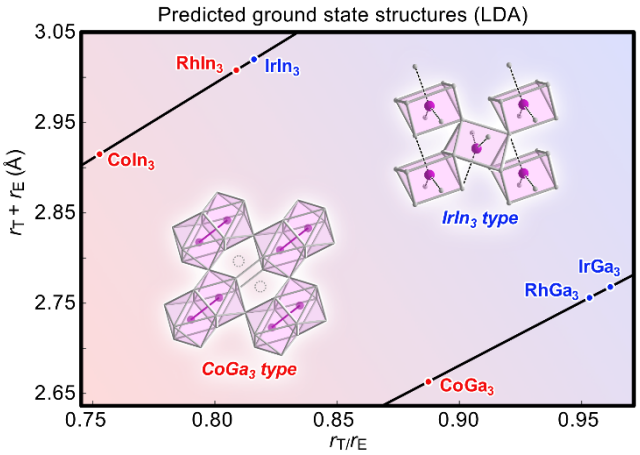

Figure 10. Structure map for 18 electron TE_3 compounds adopting the $CoGa_3$ or $IrIn_3$ structure types. The sum of the radii ($r_T + r_E$) and radius-ratio (r_T/r_E) are plotted along the *y*- and *x*-axes, respectively. Compounds for which the LDA-DFT total energy of the $CoGa_3$ or $IrIn_3$ type are lower are marked in red or blue, respectively.

ASSOCIATED CONTENT

Additional computational details; selected DFT-raMO functions for $CoGa_3$- and $IrIn_3$-type $IrIn_3$; selective COHP analysis of $CoGa_3$-type $IrIn_3$; additional images of the CP features of $CoGa_3$-type $IrIn_3$, showing interactions between neighboring layers; electronic DOS distributions and CP schemes of $CoGa_3$- and $IrIn_3$-type $IrIn_3$ for electronic structures including spin-orbit coupling. The Supporting Information is available free of charge at http://pubs.acs.org.

Interactive DFT-CP schemes and other computational details are available on the Intermetallic Reactivity Database and can be accessed through the following digital object identifiers (DOIs):

$IrIn_3$ ($CoGa_3$ type): https://doi.org/10.48704/ird_IrIn3_HT
$IrIn_3$ ($IrIn_3$ type): https://doi.org/10.48704/ird_IrIn3_RT
$CoIn_3$ ($CoGa_3$ type): https://doi.org/10.48704/ird_CoIn3
$CoIn_3$ ($IrIn_3$ type): https://doi.org/10.48704/ird_CoIn3_IrIn3
$IrGa_3$ ($CoGa_3$ type): https://doi.org/10.48704/ird_IrGa3_HT
$IrGa_3$ ($IrIn_3$ type): https://doi.org/10.48704/ird_IrGa3_RT

AUTHOR INFORMATION

Corresponding Author

Daniel C. Fredrickson – Department of Chemistry, University of Wisconsin-Madison, Madison, Wisconsin, 53706, United States; orcid.org/0000-0002-3717-7008; Email: danny@chem.wisc.edu

Author

Amber Lim – Department of Chemistry, University of Wisconsin-Madison, Madison, Wisconsin, 53706, United States; *orcid.org/0000-0001-9893-1740*

Notes

The authors declare no competing financial interest.

ACKNOWLEDGMENT

We gratefully acknowledge the financial support of the National Science Foundation through Grant DMR-2127349. This research used computational resources supported by NSF grant CHE-0840494.

REFERENCES

(1) Pfitzner, A. Phosphorus remains exciting! *Angew. Chem. Int. Ed. Engl.* **2006**, *45*, 699-700.

(2) Goodman, N. B.; Ley, L.; Bullett, D. W. Valence-band structures of phosphorus allotropes. *Phys. Rev. B* **1983**, *27*, 7440-7450.

(3) Okudera, H.; Dinnebier, R. E.; Simon, A. The crystal structure of γ-P_4, a low temperature modification of white phosphorus. *Z. Kristallogr. - Cryst. Mater.* **2005**, *220*, 259-264.

(4) Liu, D.; Guan, J.; Jiang, J.; Tomanek, D. Unusually Stable Helical Coil Allotrope of Phosphorus. *Nano Lett.* **2016**, *16*, 7865-7869.

(5) Zhang, J. L.; Zhao, S.; Han, C.; Wang, Z.; Zhong, S.; Sun, S.; Guo, R.; Zhou, X.; Gu, C. D.; Yuan, K. D.; Li, Z.; Chen, W. Epitaxial Growth of Single Layer Blue Phosphorus: A New Phase of Two-Dimensional Phosphorus. *Nano Lett.* **2016**, *16*, 4903-4908.

(6) Taylor, R.; Walton, D. R. M. The chemistry of fullerenes. *Nature* **1993**, *363*, 685-693.

(7) Hirsch, A. The era of carbon allotropes. *Nat. Mater.* **2010**, *9*, 868-871.

(8) Ye, X.; Qi, M.; Chen, M.; Zhang, L.; Zhang, J. Zero to Three Dimension Structure Evolution from Carbon Allotropes to Phosphorus Allotropes. *Adv. Mater. Interfaces* **2023**, *10*, 2201941.

(9) Scharfe, S.; Kraus, F.; Stegmaier, S.; Schier, A.; Fässler, T. F. Zintl ions, cage compounds, and intermetalloid clusters of Group 14 and Group 15 elements. *Angew. Chem. Int. Ed. Engl.* **2011**, *50*, 3630-3670.

(10) Chen, H.; Narayan, A.; Stoumpos, C. C.; Zhao, J.; Han, F.; Chung, D. Y.; Wagner, L. K.; Kwok, W. K.; Kanatzidis, M. G. Semiconducting $Ba_3Sn_3Sb_4$ and Metallic $Ba_{7-x}Sn_{11}Sb_{15-y}$ (x = 0.4, y = 0.6) Zintl Phases. *Inorg. Chem.* **2017**, *56*, 14251-14259.

(11) Ogunbunmi, M. O.; Baranets, S.; Bobev, S. Structural Complexity and Tuned Thermoelectric Properties of a Polymorph of the Zintl Phase Ca_2CdSb_2 with a Non-centrosymmetric Monoclinic Structure. *Inorg. Chem.* **2022**, *61*, 10888-10897.

(12) McGrady, J. E.; Weigend, F.; Dehnen, S. Electronic structure and bonding in endohedral Zintl clusters. *Chem. Soc. Rev.* **2022**, *51*, 628-649.

(13) Hauble, A. K.; Ciesielski, K.; Taufour, V.; Toberer, E. S.; Kauzlarich, S. M. Thermoelectric Properties of $Ba_{2-x}Eu_xZnSb_2$, a Zintl Phase with One-Dimensional Covalent Chains. *Inorg. Chem.* **2023**, *62*, 6003-6010.

(14) Gornicka, K.; Gutowska, S.; Winiarski, M. J.; Wiendlocha, B.; Xie, W.; Cava, R. J.; Klimczuk, T. Superconductivity on a Bi Square Net in LiBi. *Chem. Mater.* **2020**, *32*, 3150-3159.

(15) Flandorfer, H.; Richter, K. W.; Hayer, E.; Ipser, H.; Borzone, G.; Bros, J.-P. The binary system In–Ir: a new investigation of phase relationships, crystal structures, and enthalpies of mixing. *J. Alloys Compd.* **2002**, *345*, 130-139.

(16) Flandorfer, H. The crystal structure of a new low temperature modification of In_3Ir. *J. Alloys Compd.* **2004**, *368*, 256-259.

(17) Pöttgen, R.; Hoffmann, R.-D.; Kotzyba, G. Structure, Chemical Bonding and Properties of $CoIn_3$, $RhIn_3$, and $IrIn_3$. *Z. Anorg. Allg. Chem.* **1998**, *624*, 244-250.

(18) Yannello, V. J.; Fredrickson, D. C. Generality of the 18-*n* Rule: Intermetallic Structural Chemistry Explained through Isolobal Analogies to Transition Metal Complexes. *Inorg. Chem.* **2015**, *54*, 11385-11398.

(19) Cardoso-Gil, R.; Carrillo-Cabrera, W.; Wagner, F. R.; Grin, Y. Low-temperature phase of Ga_3Ir: Crystal structure and chemical bonding. *Z. Anorg. Allg. Chem.* **2021**, *647*, 2181-2187.

(20) Schubert, K.; Lukas, H.; Meißner, H.; Bhan, S. Zum Aufbau der Systeme Kobalt-Gallium, Palladium-Gallium, Palladium-Zinn und verwandter Legierungen. *Int. J. Mater. Res.* **1959**, *50*, 534-540.

(21) Schubert, K.; Breimer, H.; Gohle, R.; Lukas, H. L.; Meissner, H. G.; Stolz, E. Einige strukturelle Ergebnisse an metallischen Phasen III. *Die Naturwissenschaften* **1958**, *45*, 360-361.

(22) Verchenko, V. Y.; Tsirlin, A. A. Semiconducting and Metallic Compounds within the $IrIn_3$ Structure Type: Stability and Chemical Bonding. *Inorg. Chem.* **2022**, *61*, 3274-3280.

(23) Yannello, V. J.; Lu, E.; Fredrickson, D. C. At the Limits of Isolobal Bonding: π-Based Covalent Magnetism in Mn_2Hg_5. *Inorg. Chem.* **2020**, *59*, 12304-12313.

(24) Fredrickson, D. C. DFT-Chemical Pressure Analysis: Visualizing the Role of Atomic Size in Shaping the Structures of Inorganic Materials. *J. Am. Chem. Soc.* **2012**, *134*, 5991-5999.

(25) Lu, E. D.; Van Buskirk, J. S.; Cheng, J. X.; Fredrickson, D. C. Tutorial on Chemical Pressure Analysis: How Atomic Packing Drives Laves/Zintl Intergrowth in K_3Au_5Tl. *Crystals* **2021**, *11*, 906.

(26) Sanders, K. M.; Van Buskirk, J. S.; Hilleke, K. P.; Fredrickson, D. C. Self-Consistent Chemical Pressure Analysis: Resolving Atomic Packing Effects through the Iterative Partitioning of Space and Energy. *J. Chem. Theory Comput.*, under revision.

(27) Van Buskirk, J. S.; Kraus, J. D.; Fredrickson, D. C. The Intermetallic Reactivity Database: Compiling Chemical Pressure and Electronic Metrics toward Materials Design and Discovery. *Chem. Mater.* **2023**, *35*, 3582-3591.

(28) Kresse, G.; Hafner, J. Ab initio molecular dynamics for liquid metals. *Phys. Rev. B* **1993**, *47*, 558-561.

(29) Kresse, G.; Furthmüller, J. Efficient iterative schemes for ab initio total-energy calculations using a plane-wave basis set. *Phys. Rev. B: Condens. Matter* **1996**, *54*, 11169-11186.

(30) Kresse, G.; Furthmüller, J. Efficiency of ab-initio total energy calculations for metals and semiconductors using a plane-wave basis set. *Comput. Mater. Sci.* **1996**, *6*, 15-50.

(31) Blöchl, P. E. Projector augmented-wave method. *Phys. Rev. B: Condens. Matter* **1994**, *50*, 17953-17979.

(32) Kresse, G.; Joubert, D. From ultrasoft pseudopotentials to the projector augmented-wave method. *Phys. Rev. B* **1999**, *59*, 1758-1775.

(33) Maintz, S.; Deringer, V. L.; Tchougreeff, A. L.; Dronskowski, R. Analytic Projection from Plane-wave and PAW Wavefunctions and Application to Chemical-bonding Analysis in Solids. *J. Comput. Chem.* **2013**, *34*, 2557-2567.

(34) Deringer, V. L.; Tchougreeff, A. L.; Dronskowski, R. Crystal Orbital Hamilton Population (COHP) Analysis as Projected from Plane-wave Basis Sets. *J. Phys. Chem. A* **2011**, *115*, 5461-5466.

(35) Dronskowski, R.; Blöchl, P. E. Crystal Orbital Hamilton Populations (COHP): Energy-resolved Visualization of Chemical Bonding in Solids Based on Density-functional Calculations. *J. Phys. Chem.* **1993**, *97*, 8617-8624.

(36) Nelson, R.; Ertural, C.; George, J.; Deringer, V. L.; Hautier, G.; Dronskowski, R. LOBSTER: Local orbital projections, atomic charges, and chemical-bonding analysis from projector-augmented-wave-based density-functional theory. *J. Comput. Chem.* **2020**, *41*, 1931-1940.

(37) Maintz, S.; Deringer, V. L.; Tchougreeff, A. L.; Dronskowski, R. LOBSTER: A tool to extract chemical bonding from plane-wave based DFT. *J. Comput. Chem.* **2016**, *37*, 1030-1035.

(38) *Electrum.jl*; **2022**. https://github.com/brainandforce/Electrum.jl (accessed 2022-03-31).

(39) *WaveTrans: Real-space wavefunctions from VASP WAVECAR file* **2022**. https://www.andrew.cmu.edu/user/feenstra/wavetrans/ (accessed 2022-05-31).

(40) Lim, A.; Hilleke, K. P.; Fredrickson, D. C. Emergent Transitions: Discord between Electronic and Chemical Pressure Effects in the *RE*Al_3 (RE = Sc, Y, Lanthanides) Series. *Inorg. Chem.* **2023**, *62*, 4405-4416.

(41) Gonze, X.; Jollet, F.; Abreu Araujo, F.; Adams, D.; Amadon, B.; Applencourt, T.; Audouze, C.; Beuken, J. M.; Bieder, J.; Bokhanchuk, A.; Bousquet, E.; Bruneval, F.; Caliste, D.; Côté, M.; Dahm, F.; Da Pieve, F.; Delaveau, M.; Di Gennaro, M.; Dorado, B.; Espejo, C.; Geneste, G.; Genovese, L.; Gerossier, A.; Giantomassi, M.; Gillet, Y.; Hamann, D. R.; He, L.; Jomard, G.; Laflamme Janssen, J.; Le Roux, S.; Levitt, A.; Lherbier, A.; Liu, F.; Lukačević, I.; Martin, A.; Martins, C.; Oliveira, M. J. T.; Poncé, S.; Pouillon, Y.; Rangel, T.; Rignanese, G. M.; Romero, A. H.; Rousseau, B.; Rubel, O.; Shukri, A. A.; Stankovski, M.; Torrent, M.; Van Setten, M. J.; Van Troeye, B.; Verstraete, M. J.; Waroquiers, D.; Wiktor, J.; Xu, B.; Zhou, A.; Zwanziger, J. W. Recent developments in the ABINIT software package. *Comput. Phys. Commun.* **2016**, *205*, 106-131.
(42) Gonze, X.; Amadon, B.; Anglade, P. M.; Beuken, J. M.; Bottin, F.; Boulanger, P.; Bruneval, F.; Caliste, D.; Caracas, R.; Côté, M.; Deutsch, T.; Genovese, L.; Ghosez, P.; Giantomassi, M.; Goedecker, S.; Hamann, D. R.; Hermet, P.; Jollet, F.; Jomard, G.; Leroux, S.; Mancini, M.; Mazevet, S.; Oliveira, M. J. T.; Onida, G.; Pouillon, Y.; Rangel, T.; Rignanese, G. M.; Sangalli, D.; Shaltaf, R.; Torrent, M.; Verstraete, M. J.; Zerah, G.; Zwanziger, J. W. ABINIT: First-principles approach to material and nanosystem properties. *Comput. Phys. Commun.* **2009**, *180*, 2582-2615.
(43) Gonze, X. A brief introduction to the ABINIT software package. *Z. Kristallogr. - Cryst. Mater.* **2005**, *220*, 558-562.
(44) Gonze, X.; Beuken, J. M.; Caracas, R.; Detraux, F.; Fuchs, M.; Rignanese, G. M.; Sindic, L.; Verstraete, M.; Zerah, G.; Jollet, F.; Torrent, M.; Roy, A.; Mikami, M.; Ghosez, P.; Raty, J. Y.; Allan, D. C. First-principles computation of material properties: the ABINIT software project. *Comput. Mater. Sci.* **2002**, *25*, 478-492.
(45) Hartwigsen, C.; Goedecker, S.; Hutter, J. Relativistic separable dual-space Gaussian pseudopotentials from H to Rn. *Phys. Rev. B* **1998**, *58*, 3641-3662.
(46) Berns, V. M.; Engelkemier, J.; Guo, Y.; Kilduff, B. J.; Fredrickson, D. C. Progress in Visualizing Atomic Size Effects with DFT-Chemical Pressure Analysis: From Isolated Atoms to Trends in AB_5 Intermetallics. *J. Chem. Theory. Comput.* **2014**, *10*, 3380-3392.
(47) Mitchell Warden, H. E.; Voyles, P. M.; Fredrickson, D. C. Paths to Stabilizing Electronically Aberrant Compounds: A Defect-Stabilized Polymorph and Constrained Atomic Motion in $PtGa_2$. *Inorg. Chem.* **2018**, *57*, 13880-13894.
(48) A more comprehensive COHP analysis on the Ir-In interactions in this compound has been performed by Verchenko et. al (see ref. 22).
(49) Fultz, B. Vibrational thermodynamics of materials. *Prog. Mater Sci.* **2010**, *55*, 247-352.
(50) Engelkemier, J.; Fredrickson, D. C. Chemical Pressure Schemes for the Prediction of Soft Phonon Modes: A Chemist's Guide to the Vibrations of Solid State Materials. *Chem. Mater.* **2016**, *28*, 3171-3183.
(51) Kamp, K. R.; Fredrickson, D. C. A Tour of Soft Atomic Motions: Chemical Pressure Quadrupoles Across Transition Metal–Main Group 1:2 Structure Types. *Chem. Mater.* **2022**, *34*, 10011-10024.
(52) Bartel, C. J. Review of computational approaches to predict the thermodynamic stability of inorganic solids. *J. Mater. Sci.* **2022**, *57*, 10475-10498.
(53) Hlukhyy, V.; Hoffmann, R.-D.; Pöttgen, R. The Solid Solution $Mg_xIn_{3-x}Ir$ — Formation of the $FeGa_3$ Type up to x = 0.73 and the Cementite Structure with x = 0.92. *Z. Anorg. Allg. Chem.* **2004**, *630*, 68-74.
(54) Viklund, P.; Lidin, S.; Berastegui, P.; Häussermann, U. Variations of the $FeGa_3$ Structure Type in the Systems $CoIn_{3-x}Zn_x$ and $CoGa_{3-x}Zn_x$. *J. Solid State Chem.* **2002**, *165*, 100-110.
(55) Popova, S. V. New Gallides and Germanides of Transition Metals. *Phys. Scr.* **1982**, *T1*, 131-133.
(56) Likhanov, M. S.; Verchenko, V. Y.; Gippius, A. A.; Zhurenko, S. V.; Tkachev, A. V.; Wei, Z.; Dikarev, E. V.; Kuznetsov, A. N.; Shevelkov, A. V. Electron-Precise Semiconducting $ReGa_2Ge$: Extending the $IrIn_3$ Structure Type to Group 7 of the Periodic Table. *Inorg. Chem.* **2020**, *59*, 12748-12757.
(57) Bergerhoff, G.; Hundt, R.; Sievers, R.; Brown, I. D. The inorganic crystal structure data base. *J. Chem. Inf. Comput. Sci.* **1983**, *23*, 66-69.

For Table of Contents Use Only

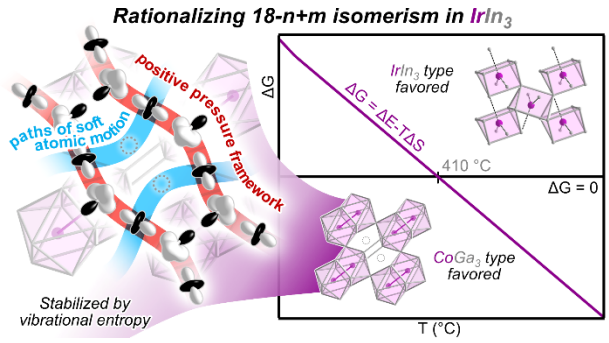

Synposis: The 18-*n* rule for intermetallics offers a variety of potential interatomic connectivity patterns for any given electron count. We investigate this question as it relates to the two polymorphs of $IrIn_3$, both of which can be interpreted in terms of the 18-*n* rule but with different electron configurations. DFT-Chemical Pressure analysis reveals how the competition between global and local packing can shape how a structure realizes the 18-*n* rule, and how temperature influences this balance.